Virologica Sinica 40 (2025) 260–274

Contents lists available at ScienceDirect

Virologica Sinica

journal homepage: www.keaipublishing.com/en/journals/virologica-sinica
www.virosin.org

Research Article

Qingqi Guxue Decoction induces S cell cycle arrest to inhibit replication of severe fever with thrombocytopenia syndrome virus

Xixi Shi [a,1], Zining Wang [a,1], Zixiang Liu [a,1], Qinting Lin [a], Mengqian Huang [a], Tze Yean Lim [a], Xiaoyan Li [b,c], Tao Wang [a,c,*]

[a] School of Life Sciences, Tianjin University, Tianjin 300110, China
[b] Tianjin Centers for Disease Control and Prevention, Tianjin 300022, China
[c] Tianjin Key Laboratory of Pathogenic Microbiology of Infectious Disease, Tianjin 300011, China

ARTICLE INFO

Keywords:
Qingqi Guxue decoction (QQGX)
Severe fever with thrombocytopenia syndrome virus (SFTSV)
Traditional Chinese medicine (TCM)
Cell cycle
S arrest

ABSTRACT

Severe fever with thrombocytopenia syndrome (SFTS) is a novel emerging acute infectious disease caused by severe fever with thrombocytopenia syndrome virus (SFTSV), characterized by high fever and thrombocytopenia. It has been proved that traditional Chinese medicine (TCM) has displayed definite therapeutic effects on viral hemorrhagic fever, indicating its potential to treat SFTS. In this study, SFTS-relative key targets were predicted via gene ontology (GO) analysis and kyoto encyclopedia of genes and genomes (KEGG) enrichment analysis. Molecular docking was then used to select stable binders. Molecules matched TCMs were identified, and a new prescription, Qingqi Guxue decoction (QQGX), was formulated to clear heat and nourish blood, with a resulting drug composition network. We explored the optimal drug proportion for QQGX. Through an in-depth study of molecular mechanisms, we found that QQGX induces S phase arrest by promoting the degradation of cyclin A2 (CCNA2) and cyclin-dependent kinase 2 (CDK2), thereby inhibiting SFTSV replication. Finally, we verified the effectiveness and safety of QQGX based on the mouse liver bile duct organoid model infected with SFTSV. In summary, our study prepared a TCM decoction using the method of network pharmacology. This decoction has a significant inhibitory effect on the replication of SFTSV and provides a new treatment strategy for hemorrhagic fever with TCM.

INTRODUCTION

Severe fever with thrombocytopenia syndrome (SFTS) is a tick-borne infectious disease caused by a novel bunyavirus, severe fever with thrombocytopenia syndrome virus (SFTSV). The clinical manifestations include high fever, gastrointestinal symptoms, liver and kidney dysfunction. Clinical studies have shown that cytokine storms, characterized by the high-level production of certain cytokines, are associated with severe forms of SFTSV infection (Sun et al., 2012). SFTSV is an enveloped virus with a negative stranded RNA genome consisting of three segments: large segment (L), medium segment (M), and small segment (S). Currently, SFTSV has been listed as one of the pathogens urgently needed for human research by the World Health Organization (WHO) (Gu et al., 2022).

For the treatment of SFTS, non-specific treatments such as blood transfusion, taking antipyretic medication, and injecting granulocyte colony-stimulating factors (G-CSF) are commonly used (Seo et al., 2021). Some specific therapies are also under development. An antiviral drug, such as ribavirin (Lu et al., 2015) has been validated to reduce the SFTSV load in patients. Another antiviral drug, favipiravir showed significant effects on reducing SFTSV load in Vero cells (Tani et al., 2016). Steroid therapy can significantly improve the average 30 days survival rate of SFTS patients (Sakaguchi et al., 2019; Jung et al., 2021). However, the safety of these therapies is relatively poor, and some therapies have serious side effects (Seo et al., 2021). Monoclonal antibody (mAb) is a promising treatment for SFTS that has been proven effective in Vero cells (Guo et al., 2013; Kim et al., 2019), but its research and development costs are expensive and time-consuming.

* Corresponding author.
E-mail address: wangtaobio@tju.edu.cn (T. Wang).
[1] Xixi Shi, Zining Wang and Zixiang Liu contributed equally to this work.

https://doi.org/10.1016/j.virs.2025.03.011
Received 25 September 2024; Accepted 25 March 2025
Available online 27 March 2025

Network pharmacology is a comprehensive discipline that combines systems biology and network informatics, which is a method to discover new drug targets and molecular mechanisms by combining computational analysis with experiments and integrating plenty of information (Boezio et al., 2017). Traditional Chinese medicine (TCM), recognized as a form of complementary and alternative medicine, is widely used in China and is gaining popularity globally (Suo et al., 2016). In recent years, herbs used in TCM, have been recognized by the scientific community worldwide (Efferth et al., 2007), several of these medicinal plants make up TCM formulae. The interactions between herbs are believed to elicit synergistic effects and attain maximum therapeutic outcomes (Li et al., 2022). The therapeutic action of TCM formulas is characterized by a multi-target and multi-level approach. This aligns with the holistic, systematic, and integrative nature of network pharmacology, making it suitable for the study of the pharmacological mechanism of Chinese medicine compounds (Zhao et al., 2023). The methods of network pharmacology used in TCM research include predicting drug targets (Muhammad et al., 2018), constructing networks of TCM, understanding biological foundation of diseases and syndromes, and forecasting disease biomarkers based on biological networks (Wang et al., 2021).

TCM plays an important role in treating viral hemorrhagic fever. In the treatment of hemorrhagic fever with renal syndrome (HFRS), individual TCM therapy reduced the mortality rate to 3.7%, far lower than the 10.7% associated with individual western medicine therapy (Singh et al., 2022). A similar situation occurred in the treatment of dengue fever. Individual TCM therapy promoted faster recovery of white blood cells and platelets, shortened the duration of fever, rash and recovery periods, and had a significantly better therapeutic effect than individual western medicine therapy (Su et al., 2025). Prescriptions recorded in some TCM classics, such as Yinqiao Powder and Ganlu Xiaodu Pill (Wu et al., 2024), have been confirmed to have antiviral effects. Moreover, TCM has the advantages of high safety and a relatively simple development process, which can compensate for the shortcomings of existing SFTS therapies.

Cell cycle regulation is a life activity targeted by many TCMs. The components of TCMs often affect the operation of cell cycle by regulating cyclins and cyclin-dependent kinases (CDKs) (Lim and Kaldis, 2013). Similarly, many viruses have been reported to facilitate their own replication by regulating the host cell cycle, such as hepatitis B virus (HBV) (Gearhart and Bouchard, 2010) and the type 1 human immunodeficiency virus (HIV-1) (Davy and Doorbar, 2007). Therefore, regulating the cell cycle is like a game, one in which TCM and viruses are both players. Our previous research has shown that SFTSV infection-induced cell cycle arrest at the G2/M transition provides favorable conditions for SFTSV replication (Liu et al., 2020), indicating a close relationship between SFTSV replication and the cell cycle. This finding opens the possibility of antagonizing SFTSV replication by influencing the cell cycle with TCM.

In this study, we developed a novel TCM prescription, Qingqi Guxue Decoction (清气固血方, QQGX), designed to clear heat and nourish blood. Our findings revealed that luteolin, a key component of QQGX, promotes the degradation of cyclin A2 (CCNA2) and cyclin-dependent kinase 2 (CDK2), arresting cells in the S phase and effectively inhibiting the replication of SFTSV. The efficacy and safety of QQGX were further validated using SFTSV-infected mouse liver bile duct organoids. This study not only provides a promising TCM-based strategy for treating viral hemorrhagic fever but also offers a potential therapeutic option to address the threat of SFTS outbreaks.

RESULTS

Key targets were predicted and collected

According to our pre-set workflow (Fig. 1), the targets of SFTS were predicted, and 3,322 SFTS targets were identified based on the GeneCards database. We downloaded the transcriptome raw data (GSE144358) of SFTS from the GEO2R database and analyzed the differentially expressed genes and identified a total of 250 differentially expressed genes (DEGs). The Venn diagram was drawn to identify the 50 intersecting targets between the predicted SFTS targets and the results of transcriptome analysis (Fig. 2A). To further explore the relationships among the intersecting targets, GO analysis was conducted to investigate the biological processes (BP), cellular components (CC), and molecular functions (MF). The results indicated that the intersecting targets were involved in biological functions such as the cell cycle, transcription, blood cell metabolism, inflammation, immunity, and cancer-related biological functions (Fig. 2B). With a P-value <0.01, KEGG pathway analysis revealed that the intersecting targets were enriched in the following pathways: cell cycle and virus infection (Fig. 2C). Among the intersecting targets, 17 were related to the cell cycle, nine were related to blood cell metabolism, and 5 were related to transcription (Fig. 2D). To narrow down the number of targets, eight targets were selected as key targets for SFTS based on the degree of protein-protein interaction (PPI) network analysis: CCNB1, BIRC5, CDC25A, CDK2, CCNA2, CTSL, SLC4A1 and TOP2A.

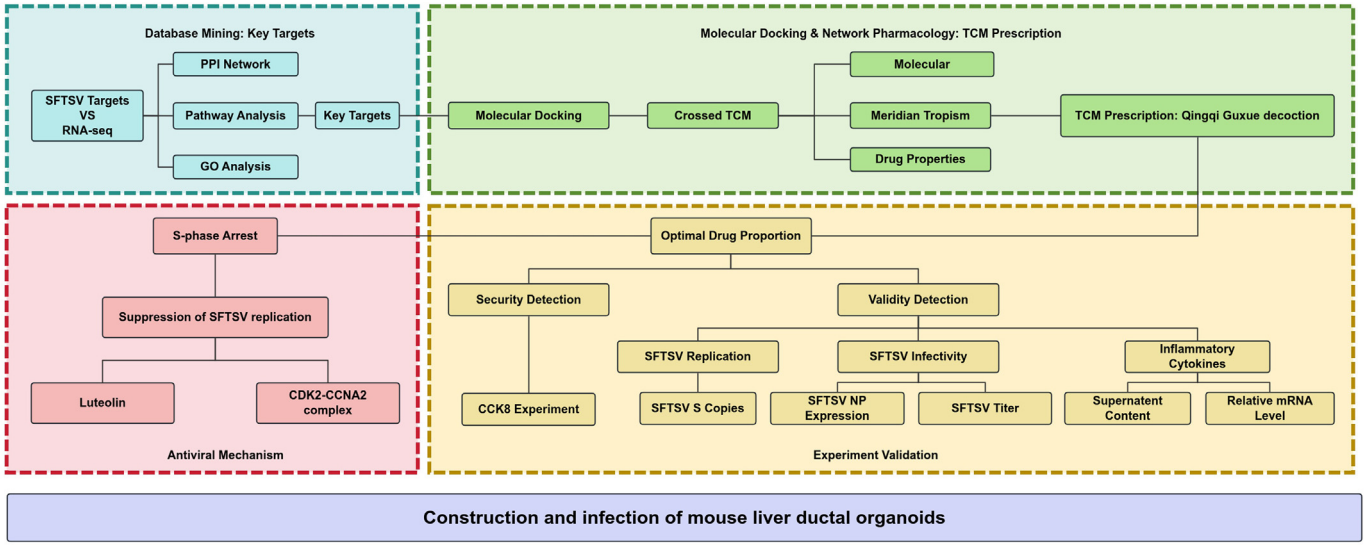

Fig. 1. The workflow of the approach used to construct the TCM prescription for SFTS treatment.

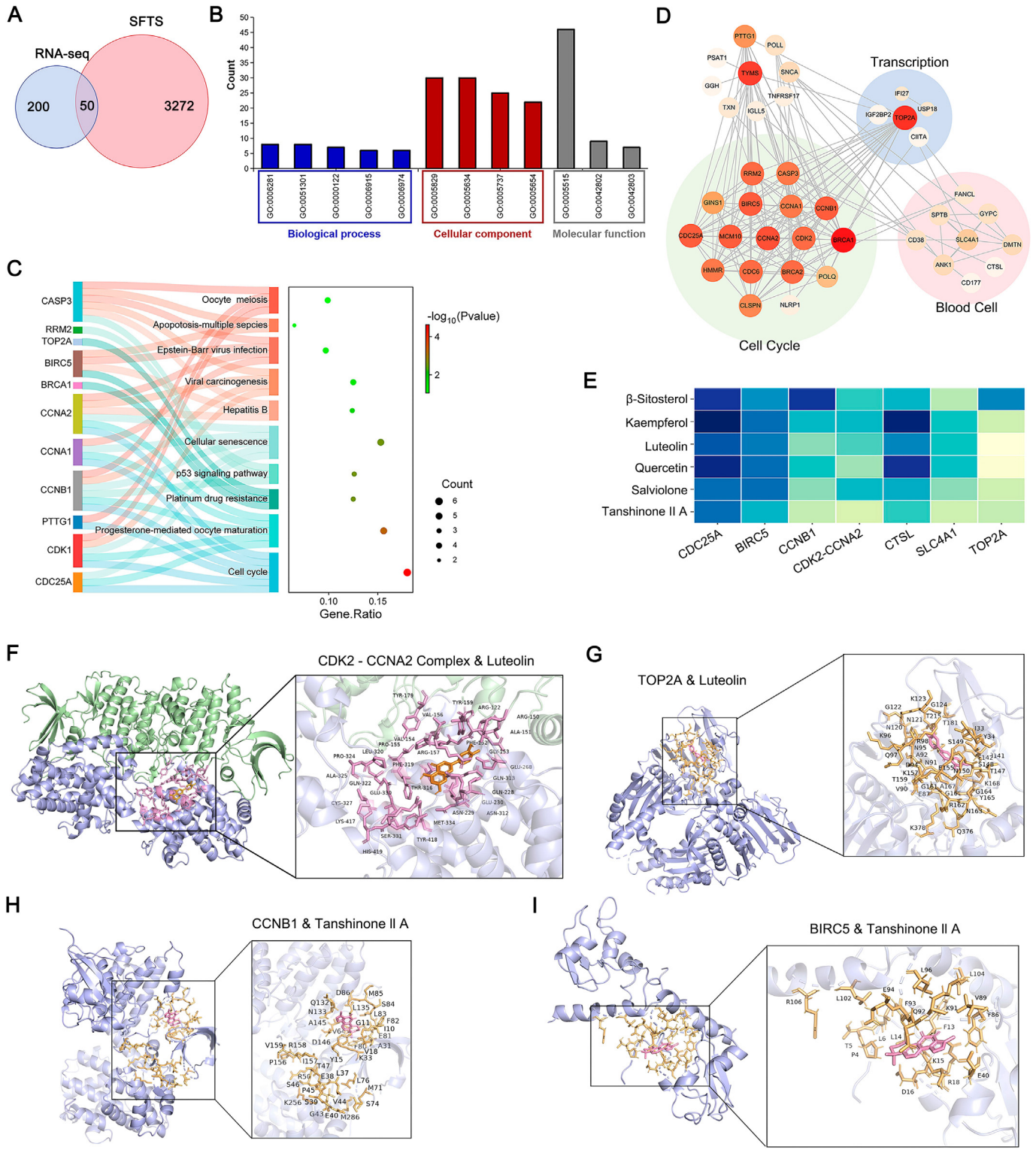

Fig. 2. Prediction of potential therapeutic targets for SFTS. **A** Venn diagram showing the intersecting targets from the transcriptome (GEO2R database, blue circle) and SFTS (Genecards database, pink circle). **B** GO enrichment analysis of the intersecting targets, including three modules of biological process (blue), cellular component (red), and molecular function (grey). The horizontal axis represents GO ID, and the vertical axis represents the number of enriched genes (Count). **C** KEGG gene enrichment pathway of the intersecting targets. The Sankey diagram represents the enrichment of genes in different pathways (colors were used to distinguish genes and pathways). In the bubble chart, the horizontal axis represents the Gene Ratio, and the vertical axis corresponds to the signaling pathway. The color of the dot represents $-\log_{10}$ (*P* value), the size of the dot represents the number of enriched genes. **D** PPI network and function of the intersecting targets. Green: Cell cycle. Pink: Blood cell. Blue: Transcription. Blank: others. The color and size of the nodes represent the PPI degree of genes (from STRING). **E** Molecular docking heatmap of β-sitosterol, kaempferol, luteolin, quercetin, salvianolone and tanshinone IIA with key targets. **F–I** The molecular docking model of CDK2-CCNA2 complex with luteolin (**F**), TOP2A with luteolin (**G**), CCNB1 with tanshinone IIA (**H**) and BIRC5 with tanshinone IIA (**I**). Template-based blind docking was used and docking forms with the lowest binding energy (below −6 kcal/mol) were selected.

Molecular docking between molecules and target proteins

TCM often contains multiple effective small molecules that regulate the expression of targets. Molecular docking is a method for drug design based on the characteristics of receptors, the interaction between receptors, and drug molecules. It can calculate the binding affinity between key targets and small molecules. Therefore, we use molecular docking to predict the corresponding small molecules from key targets in a reverse manner. Potential molecules corresponding for the key targets were selected from the TCMSP database. Through molecular docking, six molecules were identified: MOL000358 (β-Sitosterol), MOL000422 (Kaempferol), MOL000006 (Luteolin), MOL000098 (Quercetin), MOL007145 (Salviolone), and MOL007154 (Tanshinone IIA). Interestingly, CCNA2 and CDK2 regulate the S phase by forming a complex, and both targets show significant interaction and enrichment effects in our predictions. Therefore, the CDK2-CCNA2 complex has also been identified as a template for molecular docking. The molecular docking heatmap of six molecules with the key targets, including the CDK2-CCNA2 complex, is presented in Fig. 2E. Among them, the docking of luteolin with CDK2-CCNA2 complex (Fig. 2F), luteolin with TOP2A (Fig. 2G), tanshinone IIA with CCNB1 (Fig. 2H) and tanshinone IIA with BIRC5 (Fig. 2I) were stably binding, with binding energies of −9.1 kcal/mol, −10.1 kcal/mol, −8.6 kcal/mol and −8.3 kcal/mol, respectively.

Developed a TCM formula for treating SFTS

Salviolone corresponded to *Radix Salviae* and *Euphorbia helioscopia*. Tanshinone IIA corresponded to *Radix Salviae*. β-sitosterol corresponded to 245 TCMs, with 135 for kaempferol, 96 for luteolin and 189 for quercetin (Supplementary Table S1). Venn analysis was used to identify the intersection of TCMs corresponding to β-sitosterol, kaempferol, luteolin and quercetin, resulting in 23 intersecting TCMs (including *Euphorbia helioscopia*) (Fig. 3A). Analysis of the drug properties (Fig. 3B) and channel tropism (Fig. 3C) of the intersecting TCMs revealed that they were mainly concentrated in the cold or cool properties, and the lung and liver meridians. *Lonicerae Japonicae Flos* and *Forsythiae Fructus* are both cold drugs often used as companions to treat viral infections and heat symptoms (Kuchta et al., 2022; Ding et al., 2023). *Figwort Root* is the only TCM with a cold property and meridians including lung and liver. *Linderae Radix* has a mild property but is involved in the most abundant meridians (lung, liver, kidney, large intestine, and bladder). *Radix Salviae* is the only TCM containing tanshinone IIA, possessing a cold medicinal property and associated with the liver and heart meridians. Finally, we constructed a compound prescription consisting of *Lonicerae Japonicae Flos, Forsythiae Fructus, Radix Salviae, Linderae Radix* and *Figwort Root* (Fig. 3D). The prescription was named QQGX, and its function was to clear heat and reduce platelet loss. A drug composition target network was constructed using Cytoscape 3.10.0 (Fig. 3E).

Identify the optimal drug proportion for QQGX

The main medicines in TCM are primarily used to target specific diseases or syndromes, while auxiliary medicines complement them by enhancing therapeutic effects or addressing concurrent conditions. To optimize the drug proportions and maximize the efficacy of compound TCM formulations, we investigated the inhibitory effects of individual TCM components on SFTSV replication, with the aim of identifying the key components that significantly contribute to QQGX. For ease of reading, we have introduced standardized abbreviations for the herbal components: *Lonicerae Japonicae Flos* (JYH), *Radix Salviae* (DS), *Forsythia Fructus* (LQ), *Linderae Radix* (WY), and *Figwort Root* (XS).

After 1 h of SFTSV infection, we treated the cells with QQGX (a herbal formulation with a 1:1:1:1:1 ratio of JYH, DS, LQ, WY and XS) or with individual herbal components (JYH, DS, LQ, WY and XS) for an additional 24 h, respectively. The cells were then collected, and the copy number of SFTSV S segment was quantified using qRT-PCR. Our results demonstrated that JYH and DS exhibited the highest inhibitory effects on SFTSV, achieving approximately 60% inhibition, whereas LQ, WY, and XS showed weaker inhibitory effects (Fig. 4A). Consequently, JYH and DS were identified as the primary active components in QQGX.

Subsequently, while maintaining the total drug concentration, we optimized the formulation by adjusting the ratios of the five components to JYH: DS: LQ: WY: XS = 2:1:1:1:1 and 1:2:1:1:1, respectively. These adjustments led to a 5%–8% increase in inhibitory efficacy (Fig. 4B). Furthermore, doubling the proportions of JYH and DS (2:2:1:1:1) enhanced the inhibitory effect by approximately 10%. In contrast, doubling the proportions of the other three components (1:1:2:2:2) resulted in reduced efficacy compared to the original QQGX formulation (Fig. 4C). Given the traditional synergistic use of JYH and LQ, we doubled the proportions of JYH and LQ (2:1:2:1:1). However, this modification resulted in slightly diminished efficacy (Fig. 4D). Additional experiments involving the removal of LQ (1:1:0:1:1, Fig. 4E) or WY (1:1:1:0:1, Fig. 4F), as well as altering the proportion of XS (1:1:1:1:0, Fig. 4G), all resulted in significantly lower inhibition efficiency compared to the original QQGX formulation (1:1:1:1:1).

Through comprehensive analysis of seven different formulations, we employed ordinary least squares (OLS) regression modeling to determine the optimal component ratio (Chen et al., 2019). Given the discrete nature of our experimental data, we used the Kendall correlation coefficient to evaluate model fit. Our analysis revealed that the optimal ratio for the five components (JYH, DS, LQ, WY, and XS) was 2:2:1:1:1 (Fig. 4H). This optimized formulation represents a scientifically validated composition of QQGX for maximal inhibition of SFTSV.

The pharmacodynamic effects of QQGX

The curve of cell viability and QQGX concentration in four cell lines of HEK-293T, HepG2, Huh7 and THP-1 were obtained using the CCK8 assay. The cell viability decreased with increasing QQGX concentrations, ranging from 0 to 110 mg/mL. Importantly, the two experimental concentrations of QQGX (5 mg/mL and 10 mg/mL) used in our study were both within the safe concentration range for cell viability. When the concentration of QQGX was between 0 and 20 mg/mL, the cell viability of all cell lines remained above 90%. When the concentration exceeded 110 mg/mL, the cell viability of all cell lines decreased to approximately 50% (Fig. 5A–D). We employed Western blot analysis to assess the effect of QQGX on virus replication in HEK-293T, HepG2, Huh7, and THP-1 cell lines. SFTSV NP was utilized as a marker protein to evaluate SFTSV infection efficiency across different cell lines. The results demonstrated a dose-dependent decrease in SFTSV NP protein levels across all four cell lines as the drug concentrations increased to 5 and 10 mg/mL. This observation indicates that SFTSV infection efficiency was significantly reduced with higher QQGX concentrations (Fig. 5E–H). Furthermore, we quantified SFTSV replication levels using qRT-PCR to measure SFTSV S segment expression at the same concentration gradients (5 and 10 mg/mL) under QQGX treatment. The qRT-PCR results revealed a significant dose-dependent reduction in relative SFTSV S copy numbers in HEK-293T, HepG2, Huh7, and THP-1 cell lines (Fig. 5I–L). These findings collectively demonstrate that QQGX effectively inhibits SFTSV replication in various cell lines.

To evaluate the effect of QQGX on virus titer, Vero cells were inoculated with SFTSV alone or in combination with 10 mg/mL QQGX for five days. $TCID_{50}$ was assessed using quantitative qRT-PCR, and the virus titer was calculated using the Reed-Muench method. The results revealed a significant decrease in the titer after treatment with QQGX compared to no-drug group (Fig. 5M). We further assessed the effect of QQGX on viral titers through immunostaining plaque assays. The experimental results revealed that post-infection treatment with QQGX led to a significant reduction in viral titer (Fig. 5N). These consistent findings clearly demonstrate that QQGX possesses potent antiviral activity and significantly reduces viral titers.

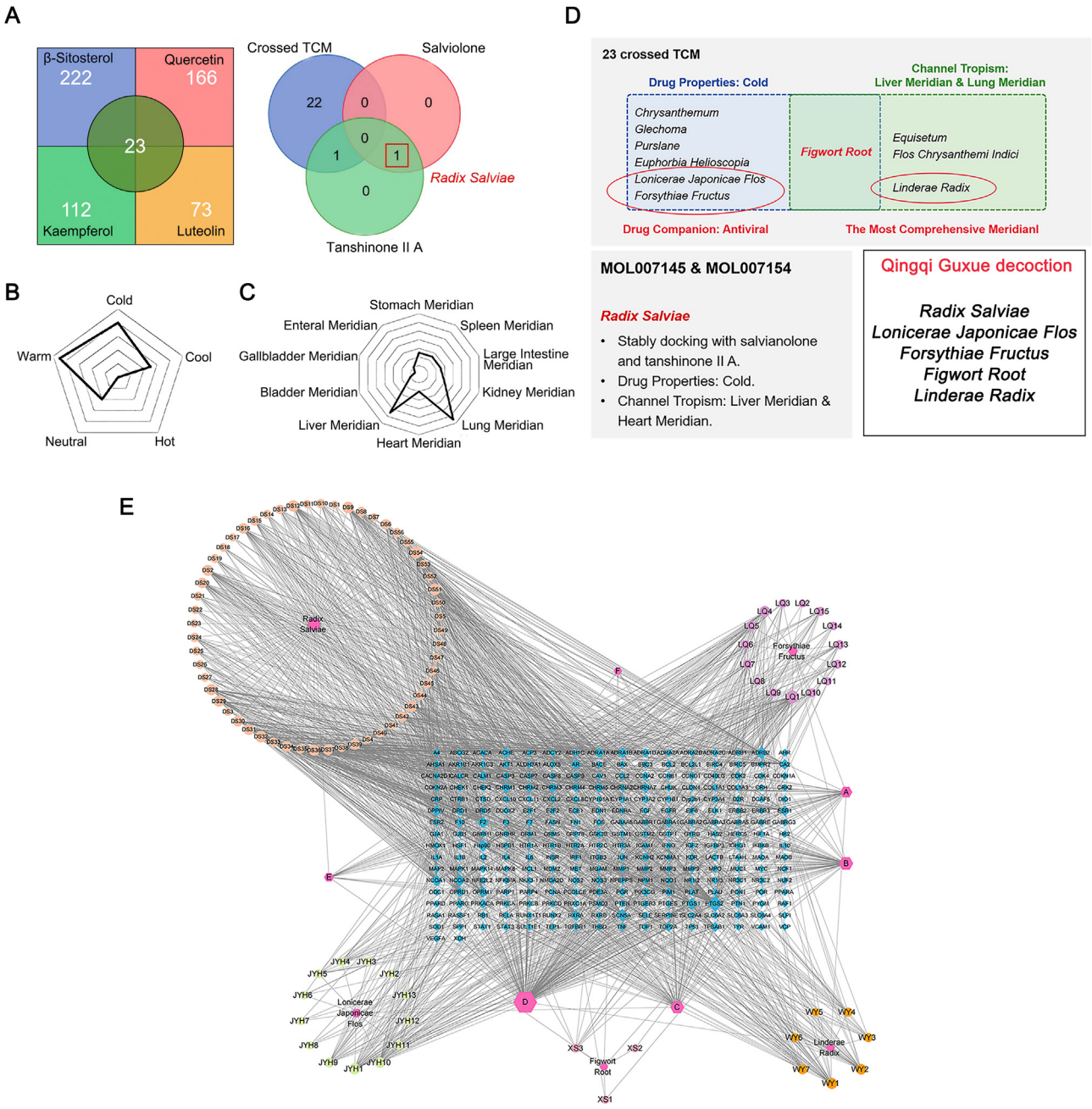

Fig. 3. Construction of Qingqi Guxue decoction (QQGX). **A** Venn analysis of molecular-relative TCMs. We performed a Venn analysis of β-sitosterol (blue), kaempferol (green), luteolin (yellow) and quercetin (pink) to identify the overlapping TCMs. Salvianolone and Tanshinone IIA correspond to a small number of TCMs, and therefore they were not included in the Venn analysis. We collected 23 TCMs corresponding to the four molecules, including two molecules related to *Radix Salviae*. **B–C** Drug properties analysis and channel tropism analysis of molecular-relative TCMs. The drug properties (**B**) and channel tropism (**C**) of TCMs were analyzed by referring to the Pharmacopoeia of the People's Republic of China (2010) and using Excel for statistical analysis. **D** Construction of QQGX. Cold drugs (represented by blue rectangles) were screened and the classical antiviral drug companion of *Lonicerae Japonicae Flos* and *Forsythiae Fructus* (represented by red circles) was selected. *Linderae Radix* (represented by a red circle) has the most extensive meridian distribution, including the liver meridian and lung meridian (represented by green rectangles), and was therefore selected to combat systemic infections caused by SFTSV. *Figwort Root* was selected due to its cold property and its association with both the liver and lung meridians (represented by the intersection of blue and green rectangles, highlighted in red). *Radix Salviae* (highlighted in red) was the only molecular that could stably dock with salvianolone and tanshinone IIA and it possesses the cold property and is associated with the liver meridian. *Lonicerae Japonicae Flos*, *Forsythiae Fructus*, *Linderae Radix*, *Figwort Root* and *Radix Salviae* were finally elected to form QQGX. **E** Drug composition targets network. The TCMs served as the central nodes, surrounded by their corresponding small molecules. The targets of QQGX were arranged in a rectangular pattern.

SFTSV is known to cause severe diseases and is highly lethal, with clinical data demonstrating that infection is accompanied by malignant inflammation and cytokine storm characteristics. To explore potential therapeutic interventions, we examined the effects of QQGX on the production of key cytokines, including IL-6, IL-10, IL-1β, and TNF-α, following SFTSV infection. Using qRT-PCR, we first measured the mRNA levels of these cytokines in HEK-293T cells. Our findings revealed a significant upregulation of IL-6, IL-10, IL-1β, and TNF-α post-SFTSV infection, aligning with established literature. Subsequent treatment with QQGX markedly inhibited the mRNA expression of these cytokines, demonstrating its potential to modulate cytokine responses at the transcriptional level (Fig. 5O). To further substantiate these observations, we

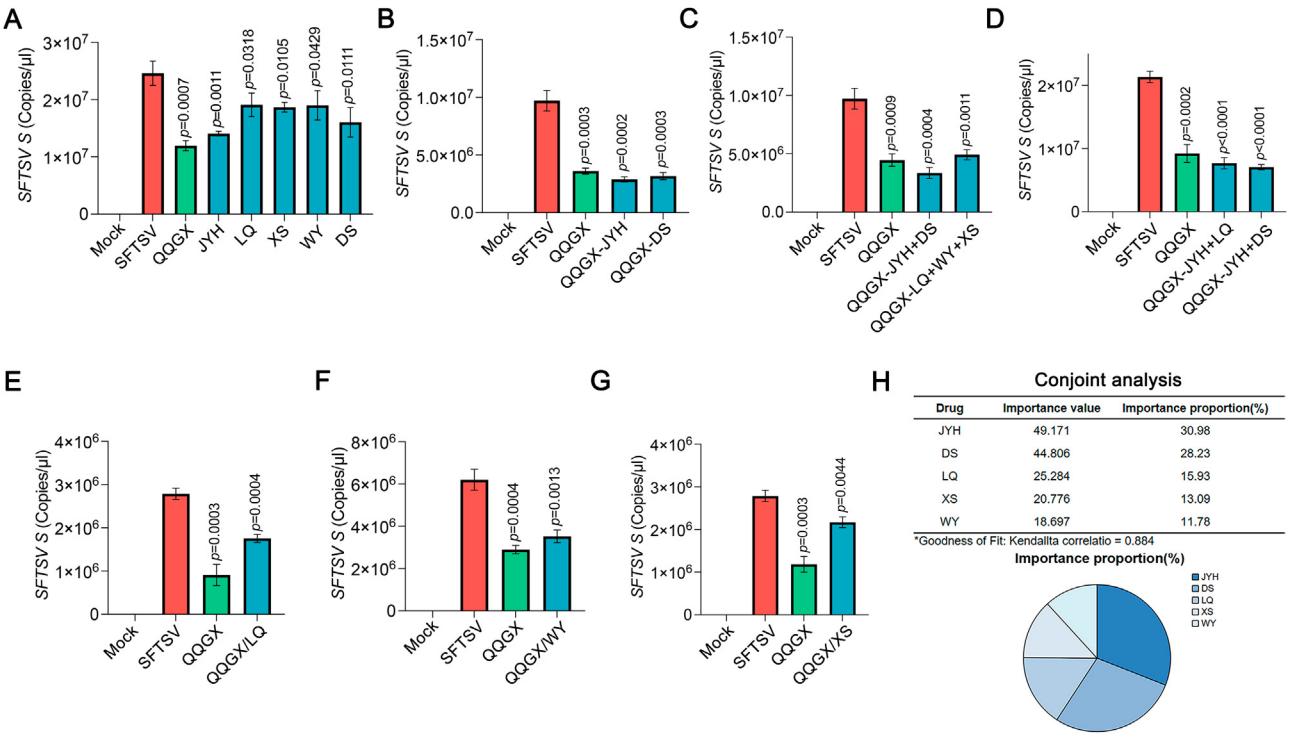

Fig. 4. Identification of the main and auxiliary components in QQGX. **A** HEK-293T cells were infected with SFTSV (MOI = 1) for 1 h, then were treated with five monotherapy agents, *Lonicerae Japonicae Flos* (JYH), *Radix Salviae* (DS), *Forsythia Fructus* (LQ), *Linderae Radix* (WY), and *Figwort Root* (XS), respectively (10 mg/mL, 50 μL) for 24 h. The inhibitory efficiency on SFTSV S segment copy number was measured by qRT-PCR. **B** After HEK-293T cells were infected with SFTSV (MOI = 1) for 1 h, JYH: DS: LQ: WY: XS (10 mg/mL, 50 μL) was administered at ratios of 2:1:1:1:1 and 1:2:1:1:1 for 24 h, with JYH: DS: LQ: WY: XS (10 mg/mL, 50 μL) in a ratio of 1:1:1:1:1 as a positive control. The copy number of SFTSV S segment was quantified using qRT-PCR. **C** HEK-293T cells were infected with SFTSV (MOI = 1) for 1 h, followed by treatment with JYH: DS: LQ: WY: XS (10 mg/mL, 50 μL) in ratios of 2:2:1:1:1 or 1:1:2:2:2 for 24 h, with JYH: DS: LQ: WY: XS (10 mg/mL, 50 μL) in a ratio of 1:1:1:1:1 as a positive control. The copy number of SFTSV S segment was quantified using qRT-PCR. **D** HEK-293T cells were infected with SFTSV (MOI = 1) for 1 h, followed by treatment with JYH and LQ at a double ratio (2:1:2:1:1, 10 mg/mL, 50 μL) for 24 h. Positive controls included JYH: DS: LQ: WY: XS at ratios of 1:1:1:1:1 and 2:2:1:1:1 (10 mg/mL, 50 μL). The copy numbers of SFTSV S segment were measured using qRT-PCR. **E–G** After HEK-293T cells were infected with SFTSV (MOI = 1) for 1 h, 50 μL 10 mg/mL JYH: DS: LQ: WY: XS (1:1:0:1:1) (**E**), JYH: DS: LQ: WY: XS (1:1:1:0:1) (**F**), or JYH: DS: LQ: WY: XS (1:1:1:1:0) (**G**) was administered for 24 h, with JYH: DS: LQ: WY: XS (1:1:1:1:1,10 mg/mL, 50 μL) as a positive control. The copy number of SFTSV S segment was measured using qRT-PCR. Data was mean ± SD. The two-tailed Student's unpaired *t*-test was used to determine statistical significance. **H** Conjoint analysis with OLS regression was performed to determine the optimal ratio that accurately reflects the five individual components in QQGX.

collected cell supernatants and employed ELISA to quantify cytokine levels. The results consistently showed that QQGX significantly reduced the concentrations of IL-6, IL-10, IL-1β, and TNF-α in the supernatants of HEK-293T cells (Fig. 5P). To ensure the robustness of our findings, we extended our investigation to THP-1 cells. Utilizing qRT-PCR and ELISA, we confirmed that QQGX similarly downregulated the levels of these cytokines in THP-1 cells (Fig. 5Q and R). Collectively, our study provides compelling evidence for the dual efficacy of QQGX, highlighting its potent antiviral and anti-inflammatory properties. These findings underscore the therapeutic potential of QQGX in mitigating the severe inflammatory responses associated with SFTSV infection.

QQGX suppresses SFTSV replication by inducing S-phase arrest in the cell cycle

The cell cycle status of the host cell often plays a critical role in viral replication (Feuer et al., 2002). When studying the impact of viruses on the host cell cycle, errors often occur due to the heterogeneity of the cell cycle stages. However, synchronizing cell populations and placing most cells in relatively similar stages of the cell cycle can effectively validate the impact of viral infection on the cell cycle. To further investigate the effect of SFTSV infection on the cell cycle, we synchronized cells in different stages, infected them with SFTSV, and then evaluated the cell cycle distribution. We found that blocking cells in the S phase could achieve antiviral effects, while blocking cells in the G2 phase could promote virus replication (Fig. 6A). Subsequently, we validated the effect of QQGX on the cell cycle. The results of flow cytometry showed that QQGX caused cell arrest in the S phase in a dose-dependent manner (Fig. 6B and C). Based on the results of Fig. 5A, we believe that QQGX may inhibit virus replication by arresting the cell cycle in the S phase.

To investigate the relative impacts of QQGX and SFTSV on the cell cycle, we treated cells with both viral infections and drugs. The results of flow cytometry showed that the number of cells in the S phase increased compared to the control group, indicating that QQGX has a greater impact on regulating the cell cycle than SFTSV, leading to a cellular environment that is unfavorable for SFTSV replication (Fig. 6D and E). QQGX is composed of five individual herbal components. Among them, *Lonicerae Japonicae Flos* and *Radix Salviae* serve as the primary ingredients, while *Forsythiae Fructus* plays a supportive role. These herbs collectively contain a small molecule known as luteolin. Additionally, cell cycle-related proteins, enriched in the SFTS database, have been identified as targets associated with luteolin (Fig. 6F). Therefore, luteolin will be the main research object in subsequent studies. As is well known, the CCNA2-CDK2 complex regulates the progression of the S phase of the cell cycle (Zhang et al., 2022). Combining the result of Fig. 2E, we speculate that luteolin may cause cell cycle arrest in the S phase by directly targeting the CCNA2-CDK2 complex. To prove this point, we used Western blot to detect the effects of QQGX and SFTSV on the expression levels of CCNA2-CDK2. The Western blot results indicated a reduction in the expression levels of CCNA2 and CDK2 upon the addition of QQGX, with a significant decrease even during viral infection (Fig. 6G). Subsequently, bio-layer interferometry (BLI) was employed to

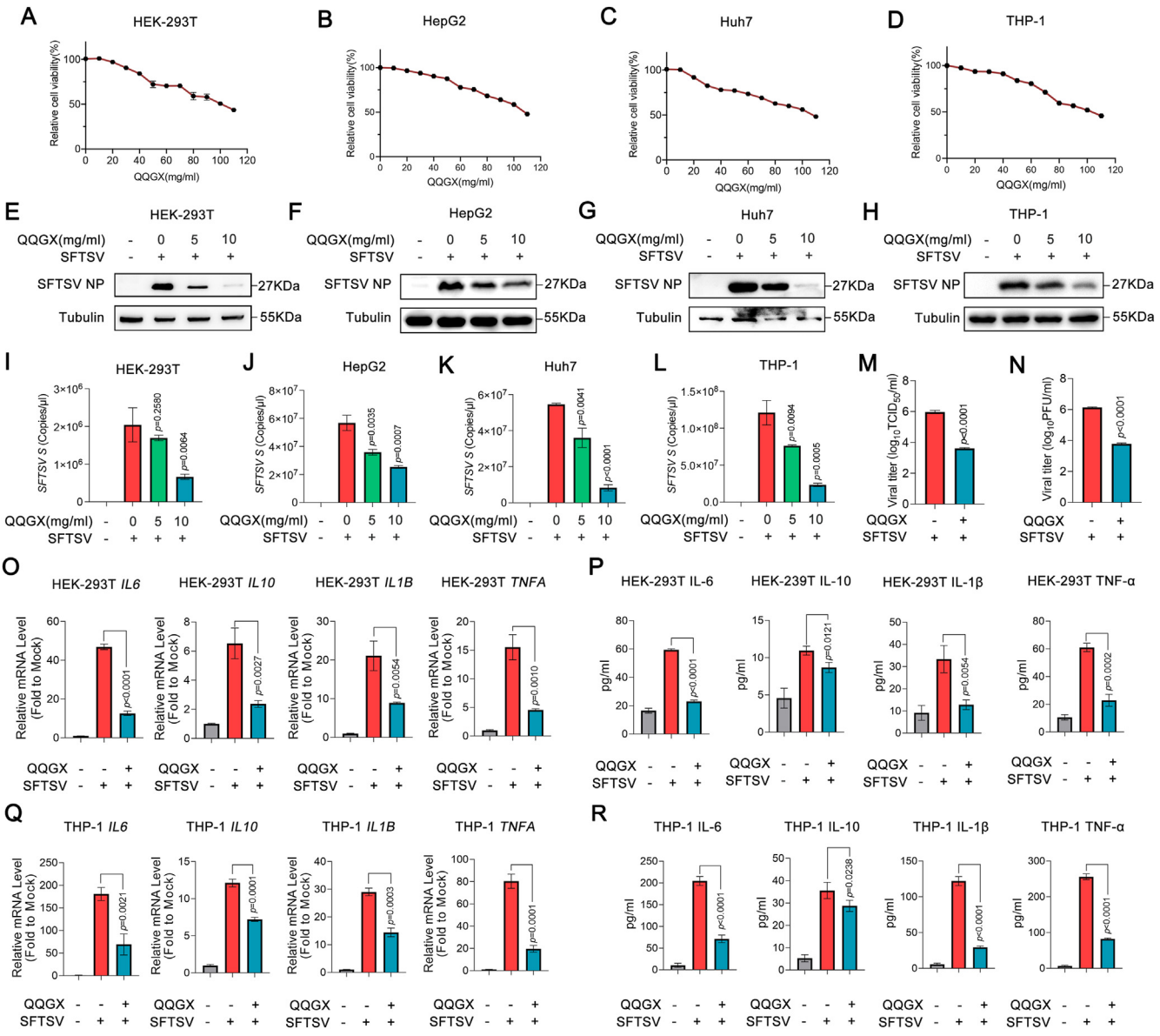

Fig. 5. Validation of QQGX's antiviral efficacy against SFTSV. **A–D** HEK-293T (**A**), HepG2 (**B**), Huh7 (**C**), and THP-1 (**D**) cells were treated with QQGX (0–110 mg/mL) for 24 h, and cell viability was measured using CCK8 experiments. **E–H** HEK-293T (**E**), HepG2 (**F**), Huh7 (**G**), and THP-1 (**H**) cells were infected with SFTSV (MOI = 1) for 1 h and treated with 5 mg/mL (25 μL) and 10 mg/mL (50 μL) QQGX for 24 h. SFTSV NP expression was detected by Western blot. **I–L** After HEK-293T (**I**), HepG2 (**J**), Huh7 (**K**), and THP-1 (**L**) cells were infected with SFTSV (MOI = 1) for 1 h, 5 mg/mL (25 μL) and 10 mg/mL (50 μL) QQGX was administered. The cells were harvested at 24 h post-treatment, and the copy number of SFTSV S segment was quantified using qRT-PCR. **M** Determination of $TCID_{50}$ for SFTSV. Vero cells were treated with 100 μL serially diluted SFTSV (MOI = 1) for 4 h, either alone or in combination with 10 mg/mL (50 μL) QQGX-containing supernatant. The treatment continued for 5 days. The $TCID_{50}$ was determined by qRT-PCR, and the virus titer was calculated using the Reed-Muench method. **N** Determination of PFU for SFTSV using immunostaining plaque assay. Vero cells were infected with 400 μL serially diluted SFTSV (MOI = 1) for 4 h. The infection was performed in the presence or absence of 10 mg/mL (50 μL) QQGX supernatant. After 5 days, viral plaques were stained with HRP-DAB, and virus titers were measured by PFUs. **O–P** After HEK-293T cells were infected with SFTSV (MOI = 1) for 1 h, 10 mg/mL (50 μL) QQGX was administered. The cells were harvested at 48 h post-treatment, and the expression levels of IL-6, IL-10, IL-1β, and TNF-α were quantified using qRT-PCR (**O**) and ELISA assay kit (**P**). **Q–R** THP-1 cells were pretreated with 10 mg/mL (50 μL) QQGX for 6 h. Subsequently, the cells were infected with SFTSV (MOI = 1) for 1 h in the continued presence of QQGX. Cells were harvested at 48 h post-treatment, and the mRNA levels of IL-6, IL-10, IL-1β, and TNF-α were quantified using qRT-PCR (**Q**) and ELISA assay kit (**R**). All the data was mean ± SD. The two-tailed Student's unpaired *t*-test was used to determine statistical significance.

determine the kinetics of CDK2/luteolin and CCNA2/luteolin interaction. In our assay, the CDK2/luteolin and CCNA2/luteolin equilibrium affinity (K_D) were 1.974E−06 and 5.181E−07, which observed that CDK2/luteolin and CCNA2/luteolin interact with high affinity (Fig. 6H and I). In summary, we found that the molecular mechanism by which QQGX antagonizes SFTSV is through the direct binding of luteolin to CCNA2 and CDK2, leading to the inhibition of virus replication by arresting the cell cycle in the S phase.

QQGX has therapeutic effects on liver ductal organoids of mouse infected with SFTSV

We verified at the cellular level that QQGX could effectively inhibit SFTSV replication. To make the findings more convincing, we cultured mouse liver ductal organoids to further verify the effect of the decoction on organoids infected with SFTSV. We used drugs that have been reported to effectively inhibit SFTSV replication as positive controls to assess the

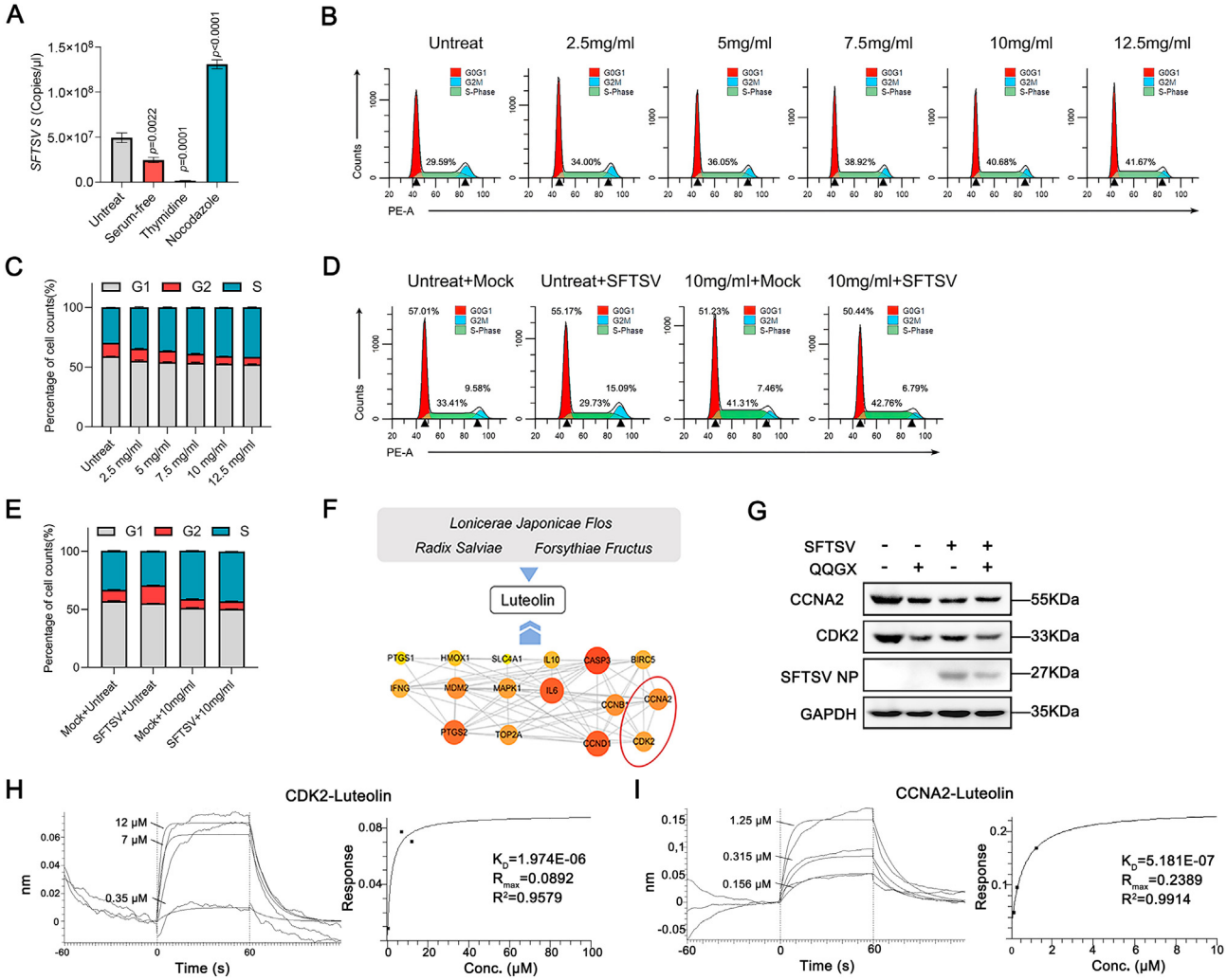

Fig. 6. QQGX inhibits SFTSV replication through cell cycle S-phase arrest. **A** HEK-293T cells were cultured under different conditions (complete medium, serum-free medium, 0.85 mM thymidine, or 50 ng/mL nocodazole) for 24 h, followed by SFTSV infection (MOI = 1) for 1 h. After 24 h of culture in complete medium, the SFTSV S segment was analyzed by qRT-PCR. **B–C** HEK-293T cells were treated with QQGX in different doses (0, 2.5, 5, 7.5, 10 mg/mL) for 24 h after infection with SFTSV (MOI = 1) for 1 h, and the number (**B**) and percentage (**C**) of G0/G1, S, and G2/M phase cells were detected using flow cytometry. **D–E** The number (**D**) and percentage (**E**) of cells in the G0/G1, S, and G2/M phases were detected using flow cytometry. Four experimental groups were established: Untreated + Mock (HEK-293T cells without treatment), Untreated + SFTSV [HEK-293T cells infected with SFTSV (MOI = 1) for 1 h, followed by replacement with fresh culture medium], 10 mg/mL + Mock [HEK-293T cells treated with 10 mg/mL (50 μL) QQGX for 24 h], 10 mg/mL + SFTSV [HEK-293T cells infected with SFTSV (MOI = 1) for 1 h, then treated with 10 mg/mL (50 μL) QQGX for 24 h]. **F** A compound-biological target network was constructed to illustrate the potential molecular mechanism of QQGX. Luteolin was identified as a core molecule that affects the S-phase by interacting with the CCNA2-CDK2 complex. The color and size of the nodes represent the degree of PPI. The PPI network was obtained from the DAVID database and visualized using Cytoscape 3.10.0. **G** HEK-293T cells underwent four different treatments: untreated cells; cells infected with SFTSV (MOI = 1) for 1 h followed by replacement with fresh culture medium; cells treated with 10 mg/mL (50 μL) QQGX for 24 h, and cells infected with SFTSV (MOI = 1) for 1 h followed by treatment with 10 mg/mL (50 μL) QQGX for 24 h. Subsequently, the cell lysates were analyzed by western blotting using antibodies against CCNA2, CDK2, SFTSV NP, and GAPDH. **H–I** BLI was used to detect the interactions between CDK2 and luteolin (**H**), as well as between CCNA2 and luteolin (**I**). K_D and R^2 were used to characterize the degree of fitting.

effectiveness of the model. Benidipine hydrochloride (BH), a calcium channel blocker (CCB), inhibited SFTSV replication *in vitro*. When the organoids grew to a size between 200 μm and 300 μm we pretreated them with 40 μM BH for 24 h to ensure that the treatment did not affect the activity of the organoids, and then they were infected with SFTSV. At each time point, ten organoids were randomly selected for tracking and imaging. The linear measurement tool in ImageJ was utilized to determine the ratio of the organoid's actual size to the scale. Subsequently, the relative growth rate of the organoid was calculated, and the data were graphically represented using Prism software. The results demonstrated that, compared to the 12-h post-infection (hpi), the relative growth rate of SFTSV-infected organoids progressively declined over time. Between 36 and 60 hpi, a gradual shrinkage of organoids was observed, culminating in the death of most organoids by 60 hpi. However, the addition of BH significantly altered this progression, with organoid death only becoming apparent at 60 hpi. This observation suggests that BH, serving as a positive control, effectively delayed SFTSV-induced organoid death (Fig. 7A and B). The results of viral RNA extracted from organoids at 60 hpi and detected via qRT-PCR demonstrated that the addition of BH significantly inhibited viral replication (Fig. 7C). The results indicated that the mouse hepatobiliary organoid model we constructed was effective. Subsequently, mature organoids were pretreated with 5 or 10 mg/mL of QQGX for 24 h, which maintained high levels of organoid viability. Following pretreatment, the organoids were infected with SFTSV for 60 h, with QQGX remaining present throughout the infection period. The results demonstrated that the relative growth rate of SFTSV-infected organoids progressively declined over time when compared to the baseline measurement at 6 hpi. Between 24 and 60 hpi, a gradual atrophy of organoids was observed, culminating in the death of

most organoids by 60 hpi. In contrast, the group treated with 5 mg/mL QQGX exhibited a delayed response, with organoids showing gradual shrinkage only at 48 hpi. While some organoids in this treatment group also died by 60 hpi, the mortality rate was significantly lower than that observed in the untreated SFTSV-infected group. The 10 mg/mL QQGX treatment group demonstrated an even more pronounced protective effect, with organoids maintaining high viability at 60 hpi. These findings indicate that QQGX can effectively mitigate SFTSV-induced organoid death in a dose-dependent manner (Fig. 7D–E). The qRT-PCR results further corroborate these findings (Fig. 7F).

To further determine at which stage QQGX can exert its inhibitory effect on SFTSV replication, we conducted a series of experiments according to the protocol schematically shown in Fig. 7G. The results indicated that compared to the baseline at 0 hpi, the relative growth rate of SFTSV-infected organoids gradually decreased over time. At 36 hpi, gradual atrophy of the organoids was observed, ultimately resulting in the death of most organoids by 60 hpi. In both scenarios, when organoids were pretreated with QQGX and when co-administered with the virus, they exhibited surface wrinkling at 36 hpi, followed by extensive cell death at 60 hpi. This demonstrated that neither QQGX pretreatment nor co-administration with the virus could mitigate SFTSV-induced organoid mortality. However, QQGX treatment during the post-infection stage effectively attenuated SFTSV-mediated damage to the organoids, with the majority maintaining high viability beyond 60 hpi (Fig. 7H and I). The qRT-PCR analysis additionally indicates that QQGX plays a positive role in the post-SFTSV infection stage. (Fig. 7J). The above results provide sufficient evidence for the therapeutic efficacy of QQGX.

DISCUSSION

SFTS, a newly emerging acute infectious disease caused by SFTSV, poses a significant threat to public health. Although several specific therapies for SFTS have been developed, their clinical application remains limited. The classic antiviral drugs, favipiravir and ribavirin, have been shown to reduce serum viral load and alleviate symptoms in SFTS patients, however, they may lead to complications such as anemia and hyperamylasemia (Lu et al., 2015; Tani et al., 2018). While hormone therapy based on steroids can eliminate inflammatory factors in patients' serum and improve the average survival rate of SFTS patients. However, it may cause severe fungal infections (Sakaguchi et al., 2019; Jung et al., 2021). As a CCB approved by the FDA, BH has been shown to inhibit the replication of various viruses, including SFTSV, however, its safety in treating SFTS remains to be fully verified (Li et al., 2019). Amodiaquine, a clinically approved drug for treating malaria with broad-spectrum antiviral effects, exhibits insufficient antiviral activity against SFTSV to warrant further clinical development (Baba et al., 2023). Recent studies have demonstrated that the anti-PD-1 nanobody NbP45 holds potential as a treatment for SFTS, however, its research and development are both costly and time-intensive (Ji et al., 2024). In summary, existing SFTS-specific therapies face issues such as low safety, significant side effects, and challenges in research and development.

Given the limitations of existing SFTS-specific therapies, we aimed to develop a novel therapy with enhanced safety. To this end, we focus on TCM therapy. TCM has played an important role in the treatment of viral hemorrhagic fevers such as HFRS and dengue fever in the past. In the treatment of HFRS, TCM therapy significantly reduced the mortality rate of patients (Sehgal et al., 2023). In the treatment of dengue fever, compared to western medicine therapy, TCM therapy can shorten the course of dengue fever and reduce patient mortality (Li and Saldanha, 2008). Therefore, TCM has the potential to treat SFTS. Traditionally, the construction of TCM prescriptions has relied heavily on extensive clinical experience and case studies, which often entail significant trial-and-error and time costs. In our research, we used a bioinformatics method based on network pharmacology and molecular docking for the construction of a TCM prescription. We constructed a compound prescription consisting of *Lonicerae Japonicae Flos*, *Forsythiae Fructus, Radix Salviae, Linderae Radix,* and *Figwort Root,* and named it QQGX. We employed conjoint analysis approach to determine the optimal ratio of five individual drugs in QQGX. Subsequent cell-based experiments were conducted to validate the therapeutic efficacy of QQGX.

Based on the enriched results of network pharmacology, we predicted potential therapeutic targets for SFTS. As mentioned earlier, CCNA2 and CDK2 are enriched in the form of a complex, and due to their strong binding ability with target molecules, they have been selected as key future research objects. However, it is well known that TCM often targets multiple molecular targets to exert its effects. Due to limited research time, we are unable to analyze the molecular mechanisms of each target individually. The other targets with high scores in our study are BIRC5, SLC4A1, and TOP2A. Here, we propose a tentative mechanism by which QQGX suppresses SFTSV replication through the regulation of these targets. BIRC5 has been proven to be an effective inhibitor of caspase (Frazzi, 2021), and the degradation of its targeted binding by QQGX may trigger early apoptosis, thereby inhibiting virus replication. SLC4A1, as a cell surface carrier protein (Yang et al., 2023), may be a potential receptor or helper protein for SFTSV infection, or its transported product is crucial for virus replication. Therefore, the targeting of SLC4A1 by QQGX may directly affect virus adsorption or indirectly affect virus replication by affecting cellular metabolism. TOP2A is a DNA topoisomerase, but there is limited research on its interaction with RNA viruses. A recent blood transcriptome analysis on COVID-19 showed a significant enrichment of TOP2A (Yan et al., 2022). Although the possible role of TOP2A in SFTSV life process is unclear, the addition of QQGX may affect the transcription process of multiple antiviral genes, thereby affecting virus replication. In the future, we will continue to focus on the molecular mechanisms by which QQGX affects other targets.

Clinical data shows that fatal SFTS patients develop a pathological state called cytokine release syndrome (Yoo et al., 2021; Kang et al., 2023). Therefore, in our study, QQGX has antiviral function in different cell lines and has also been detected to have anti-inflammatory effects, which fully demonstrates the effectiveness of QQGX on SFTSV infection. After demonstrating the antiviral and anti-inflammatory effects of QQGX in multiple cell lines, we further sought to validate its therapeutic potential in more physiologically relevant models. For this purpose, we adopted a three-dimensional (3D) organoid system. An organoid is a 3D structure formed by the self-assembly of adult stem cells derived from primary tissues *in vitro* (Corrò et al., 2020). It can differentiate into multiple organ-specific cell types, reproducing key functions and structures of real human organs *in vitro* (Dutta et al., 2017). Organoids provide a model that reflects the *in vivo* organization, operations, and genetic hallmarks of the tissues, which has propelled their use in diverse human diseases (Clevers, 2016). The liver, a main target organ for SFTSV infection (Luo et al., 2023), is usually assumed to be the major site of first-pass metabolism of orally administered drugs (Verbeeck, 2008). Consequently, interactions between SFTSV and QQGX can occur in the liver. BH is commonly used in clinics, as an anti-SFTSV compound *in vitro* (Li et al., 2019), we use BH as a positive control indicating that our constructed hepatobiliary organ model can be applied for drug efficacy testing. On this basis, we have demonstrated that QQGX can effectively inhibit the replication of SFTSV in hepatobiliary organs. It cannot be denied that organoids derived from normal tissue in mice may still exhibit differences in physiological responses to the human body. In future studies, we plan to conduct more comprehensive and in-depth investigations into the molecular mechanisms by constructing human organoids derived from induced pluripotent stem cells (iPSCs).

CONCLUSIONS

In our study, we innovatively applied TCM to treat SFTS. Using a method based on network pharmacology and molecular docking was used to develop a new TCM formula QQGX. Its inhibitory effect on SFTSV

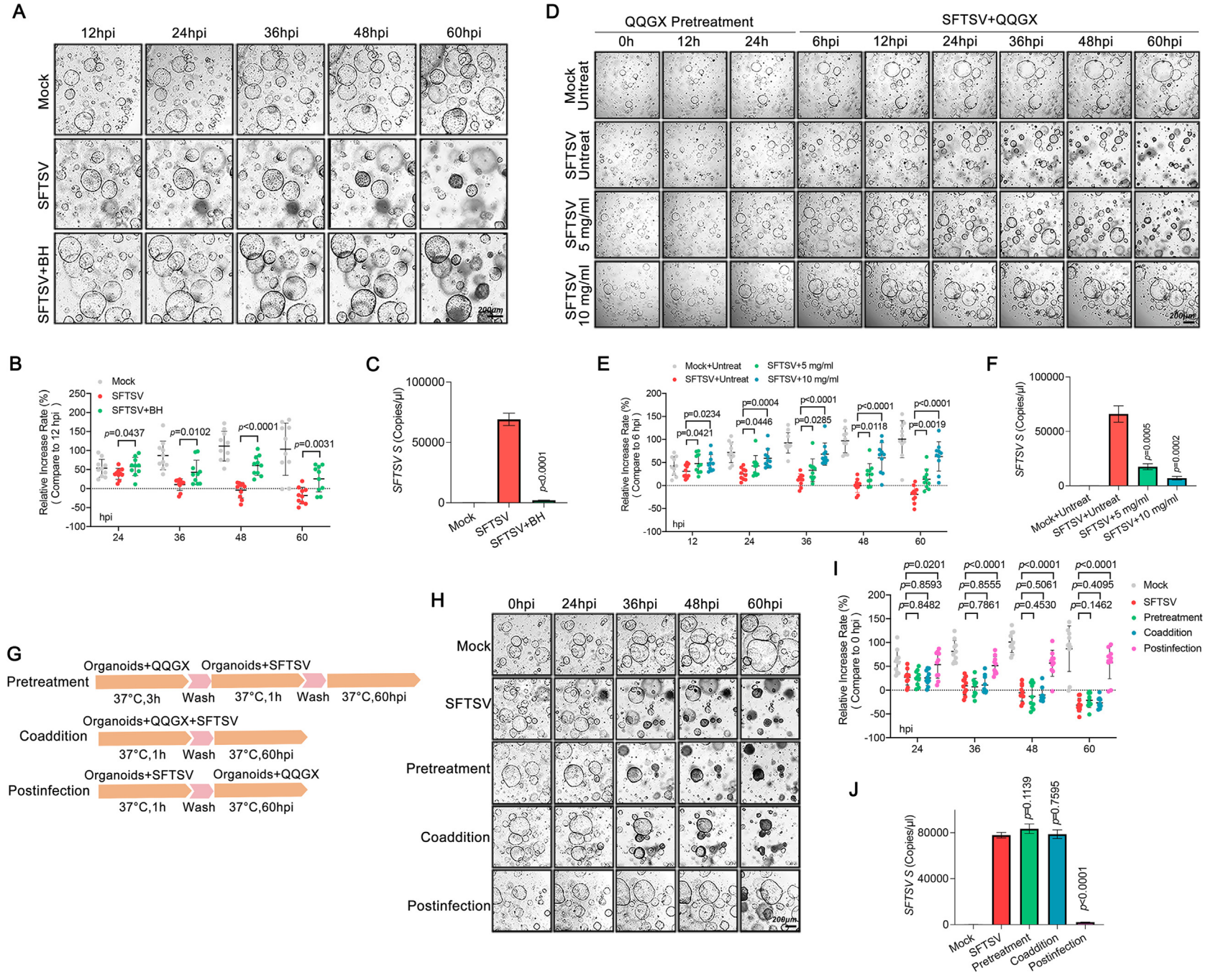
A
12hpi
24hpi
36hpi
48hpi
60hpi
Mock
SFTSV
SFTSV+BH
200μm
D
QQGX Pretreatment
SFTSV+QQGX
0h
12h
24h
6hpi
12hpi
24hpi
36hpi
48hpi
60hpi
Mock Untreat
SFTSV Untreat
SFTSV 5 mg/ml
SFTSV 10 mg/ml
200μm
B
Mock
SFTSV
SFTSV+BH
Relative Increase Rate (%) (Compare to 12 hpi)
p=0.0437
p=0.0102
p<0.0001
p=0.0031
hpi
24
36
48
60
C
SFTSV S (Copies/μl)
p<0.0001
Mock
SFTSV
SFTSV+BH
E
Mock+Untreat
SFTSV+Untreat
SFTSV+5 mg/ml
SFTSV+10 mg/ml
Relative Increase Rate (%) (Compare to 6 hpi)
p=0.0234
p=0.0421
p=0.0004
p=0.0446
p<0.0001
p=0.0285
p<0.0001
p=0.0118
p<0.0001
p=0.0019
hpi
12
24
36
48
60
F
SFTSV S (Copies/μl)
p=0.0005
p=0.0002
Mock+Untreat
SFTSV+Untreat
SFTSV+5 mg/ml
SFTSV+10 mg/ml
G
Pretreatment
Organoids+QQGX
Organoids+SFTSV
37°C,3h
Wash
37°C,1h
Wash
37°C,60hpi
Coaddition
Organoids+QQGX+SFTSV
37°C,1h
Wash
37°C,60hpi
Postinfection
Organoids+SFTSV
Organoids+QQGX
37°C,1h
Wash
37°C,60hpi
H
0hpi
24hpi
36hpi
48hpi
60hpi
Mock
SFTSV
Pretreatment
Coaddition
Postinfection
206μm
I
p=0.0201
p=0.8593
p=0.8482
p<0.0001
p=0.8555
p=0.7861
p<0.0001
p=0.5061
p=0.4530
p<0.0001
p=0.4095
p=0.1462
Relative Increase Rate (%) (Compare to 0 hpi)
hpi
24
36
48
60
Mock
SFTSV
Pretreatment
Coaddition
Postinfection
J
SFTSV S (Copies/μl)
p=0.1139
p=0.7595
p<0.0001
Mock
SFTSV
Pretreatment
Coaddition
Postinfection

Fig. 7. Verification of the antagonistic effect of QQGX on SFTSV in a mouse liver bile duct organoid model. **A–B** After 7 days of cultivation, primary organoids were passaged within 4 days, grew to 200–300 μm in diameter. They were divided into three treatment groups: untreated, infected with 50 μL SFTSV (7.2×10^7 $TCID_{50}$/mL) for 1 h followed by fresh medium replacement, and infected with 50 μL SFTSV (7.2×10^7 $TCID_{50}$/mL) for 1 h followed by BH (40 μM) treatment for 60 hpi. Bright field imaging was used to analyze liver bile duct organoids under these conditions. Scale bar, 200 μm (**A**). Ten liver bile duct organoids were randomly selected for size measurement. Organoid dimensions were quantified using the linear measurement tool in ImageJ software, using the formula: (diameter at time X – diameter at 12 hpi)/diameter at 12 hpi (**B**). **C** Mouse liver bile duct organoids were infected with 50 μL SFTSV (7.2×10^7 $TCID_{50}$/mL) for 1 h and then treated with BH (40 μM) for 60 hpi. The copy number of SFTSV S segment in the organoids was detected by qRT-PCR. **D–E** When the organ-like structures reached the fourth day of growth, they were pretreated with 10 mg/mL (50 μL) QQGX for 24 h. Subsequently, four different treatments were applied: untreated control, infected with 50 μL SFTSV (7.2×10^7 $TCID_{50}$/mL) for 1 h, followed by replacement with fresh culture medium, infected with 50 μL SFTSV (7.2×10^7 $TCID_{50}$/mL) for 1 h, followed by treatment with 5 mg/mL (25 μL) and 10 mg/mL (50 μL) QQGX for 60 hpi. Bright-field imaging was used to analyze the liver bile duct organoids under these conditions. Scale bar, 200 μm (**D**). Ten liver bile duct organoids were randomly selected for size measurement. Organoid dimensions were quantified using the linear measurement tool in ImageJ software, using the formula: (diameter at time X–diameter at 6 hpi)/diameter at 6 hpi (**E**). **F** Mouse liver bile duct organoids were infected with 50 μL SFTSV (7.2×10^7 $TCID_{50}$/mL) for 1 h and then treated with 5 mg/mL (25 μL), 10 mg/mL (50 μL) QQGX for 60 hpi. The copy number of SFTSV S segment in the organoids was detected by qRT-PCR. **G** A schematic of different QQGX treatments administered to organoids. **H–I** When the organoids reached the fourth day of culture, they were processed according to the steps outlined in Fig. 7G. Bright-field imaging was used to analyze the morphological effects of QQGX (10 mg/mL, 50 μL) on the liver bile duct organoids of mice infected with 50 μL SFTSV (7.2×10^7 $TCID_{50}$/mL, 60 hpi). Scale bar, 200 μm (**H**). Ten liver bile duct organoids were randomly selected for size measurement. Organoid dimensions were quantified using the linear measurement tool in ImageJ software, using the formula: (diameter at time X–diameter at 0 hpi)/diameter at 0 hpi. (**I**). **J** To evaluate the effect of QQGX (10 mg/mL, 50 μL) on the copy number of SFTSV S segment, qRT-PCR was performed on the liver bile duct organoids of mice infected with 50 μL SFTSV (7.2×10^7 $TCID_{50}$/mL) at 60 hpi. Data are mean ± SD. The two-tailed Student's unpaired *t*-test was used to determine statistical significance. **B**, **E**, **I** The data were graphically represented using Prism software. Data are mean ± SD. The multiple *t*-test was used to determine statistical significance.

was subsequently validated through cell and organoid experiments. QQGX promotes the degradation of CCNA2 and CDK2, leading to cell cycle arrest at the S phase and suppression of SFTSV replication. This provides new insights for SFTS treatment (Fig. 8).

MATERIALS AND METHODS

Intersecting targets selection

GeneCards Database Search: The GeneCards database integrates gene-centric data from approximately 150 online resources, encompassing genomic, transcriptomic, proteomic, genetic, clinical, and functional information. We first search for all targets related to SFTS in GeneCards to obtain all disease targets related to SFTS, we performed the following steps: Login to GeneCards database (https://www.genecards.org/). Enter the full name of SFTS (Severe Fever with Thrombocytopenia Syndrome) in the "Search GeneCards" search bar in the upper right corner of the page to obtain the disease targets. In this process, we should filter the results by selecting "Protein Coding" under the "Category" option to ensure relevance to protein-coding genes. This initial search yielded 3322 SFTS-related disease targets (Supplementary Table S2).

Transcriptomic Data Integration: To enhance the accuracy of target prediction, we complemented the GeneCards data with transcriptomic analysis also using a dataset from the GEO2R database. Obtaining 250 transcriptomic targets from the GEO2R analysis (Supplementary Table S3). Performing a Venn analysis to identify overlapping targets between the GeneCards-derived 3322 SFTS targets and 250 transcriptomic targets, resulting in 50 intersecting targets. Among them, 3272 genes are enriched in SFTS disease targets, but do not exist in transcriptomes.

Protein-protein interaction data

Human PPI data of the intersecting targets were derived from STING (http://cn.string-db.org) using the "Multiple Proteins by Identifiers" tool, and the network analysis was performed using Cytoscape 3.10.0. The color and size of the nodes represented the PPI degree of the targets.

Prediction of the key targets

Signal pathway enrichment and GO analysis were conducted using the Functional Annotation Tool in the DAVID database (https://david.ncifcrf.gov/). The BP, CC, and MF of the genes were predicted, and the DAVID database provided partial information on gene enrichment pathways. Additionally, KEGG pathway analysis was performed using the KOBAS website (http://kobas.cbi.pku.edu.cn/), and pathway enrichment analysis was carried out via the KEGG database (https://www.kegg.jp/) to obtain detailed information on gene enrichment pathways. Based on the GO analysis, pathway analysis, and gene differential expression levels, eight key targets were identified from the intersecting targets.

Molecules database searching

The molecules corresponding to the key targets were filtered using the TCMSP, which can be accessed at http://tcmspw.com/tcmsp.php. The data filtering was conducted based on the following criteria: (1) oral bioavailability of at least 30%; (2) drug similarity of at least 0.18.

Molecular docking

The protein sequences of CCNB1 (PDB ID: 6GU2), BIRC5 (PDB ID: 1XOX), TOP2A (PDB ID: 1ZXM), CDC25A (PDB ID: 1C25), SLC4A1 (PDB ID: 8E34), CTSL (PDB ID: 7W33), and CDK2-CCNA2 complex (PDB ID: 7MKX) were downloaded from PDB database (https://www.rcsb.org). The sequences of molecules were downloaded from TCMSP database. The protein sequences, as well as molecule sequences, were then input

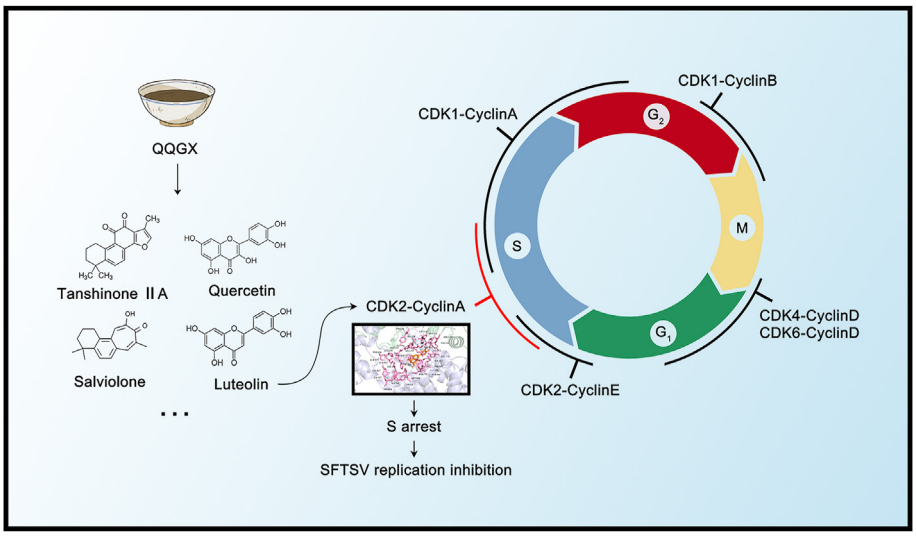

Fig. 8. Proposed model for QQGX induced S-phase arrest. QQGX contains the small molecule luteolin, which specifically binds to the cell cycle protein CDK2-CCNA2 complex, resulting in cell cycle arrest in the S phase and inhibiting SFTSV replication.

into Swissdock database (http://www.swissdock.ch/) for template based blind docking. The docking combinations with the lowest free energy below −6 kcal/mol were considered stable dockings. Molecules capable of stably docking with all key targets were selected. Finally, PyMOL 3.0 software was used for further drawing.

Construction of QQGX decoction

The molecule corresponding TCMs were searched from TCMSP database and a Venn analysis was conducted to identify intersecting TCMs. The medicinal properties and meridian tropism of the intersecting TCMs were acquired in the Pharmacopoeia of the People's Republic of China and used to construct the TCM prescription. The newly constructed TCM prescription was named QQGX (Supplemental Table S4).

Network construction

The component-target network of QQGX was constructed using Cytoscape 3.10.0. The target genes were labeled as "gene" and filled with blue, while the QQGX components were labeled as "Type". The size of the nodes was determined based on the degree obtained from the network analysis. The relationship between genes and small molecules, as well as between small molecules and TCM, is integrated into a "network", and the attributes of small molecules, TCM, and genes are integrated into a "Type". (Supplemental Table S4).

Preparation of QQGX

Radix Salviae, *Lonicera japonica Flos*, *Forsythiae Fructus*, *Linderae Radix* and *Figwort Root* were purchased from Tianjin Baicao Tang. 0.4 g of *Radix Salviae* and *Lonicera japonica Flos,* and 0.2 g of *Forsythiae Fructus*, *Linderae Radix* and *Figwort Root* were ground into a powder. Twenty milliliters of sterile water were added to dissolve the powder to obtain a suspension. After boiling for 30 min, the suspension was filtered through a 0.45 μm filter membrane to obtain the aqueous solution of QQGX (2:2:1:1:1) at a concentration of 100 mg/mL. The preparation methods for single component suspensions and different proportions of QQGX were similar.

Viruses and cell lines

The SFTSV strain HB29 (NCBI Taxonomy ID: 992212, NC_018136, NC_018138, NC_018137) was provided by Dexin Li at the Chinese Center for Disease Control and Prevention. The virus was cultured in Vero cells for 7 days, and the culture supernatant was collected to harvest the virus. HEK-293T, Vero, THP-1 and HepG2 cells were purchased from the American Type Culture Collection (ATCC). The Huh7 cells were kindly provided by Dr. Huahao Fan at the School of Life Sciences, Tianjin University. HEK-293T, Vero and Huh7 cells were cultured in DMEM medium (Gibco, USA, C11995500BT) supplemented with 10% fetal bovine serum (FBS) (ExCell Bio, China, FCS500) and 1% antibiotic-antimycotic (Cytiva, USA, SH40003). HepG2 and THP-1 cells were cultured in RPMI 1640 medium (Gibco, USA, 11875093) supplemented with 10% FBS and 1% antibiotic-antimycotic. The cells were cultured at 37 °C in a 5% CO_2 incubator.

Individual TCM treatment and optimal TCM proportion

The water extracts of five traditional Chinese medicines were prepared, each at a concentration of 100 mg/mL. HEK-293T cells were infected with SFTSV (MOI = 1) for 1 h, and then the five individual drugs were separately added in infected cells for 24 h (10 mg/mL, 50 μL). The effect of each drug on the copy number of SFTSV S segment was measured using qRT-PCR. To explore the optimal combination of QQGX for inhibiting SFTSV replication, we prepared 50 μL different drug ratios by mixing the water extracts while maintaining a total concentration of 10 mg/mL. HEK-293T cells were infected with SFTSV (MOI = 1) for 1 h and then treated with the different drug ratios for 24 h. The effect of these drug ratios on the copy number of SFTSV S segment was assessed using qRT-PCR. Conjoint analysis was presented by SPSSAU platform (https://spssau.com/) to calculate the importance proportion of each drug. The OLS model was used to predict importance values, and the Kendall's tau correlation was used to assess the goodness of fit.

CCK8 experiment to detect the cytotoxicity of QQGX

HEK-293T, HepG2, Huh7, and THP-1 cells were seeded onto a 96-well plate and cultured for 24 h. QQGX was prepared at various concentrations (10, 20, 30, 40, 50, 60, 70, 80, 90, 100, 110 mg/mL), and then the original culture medium was replaced with the QQGX solutions at the respective concentrations. After 24 h, CCK8 solution was added to the cells and cultured for 1 h. The absorbance at 450 nm (A450) was detected using a microplate reader, and the IC_{50} was then calculated using GraphPad Prism.

Western blot detection

After infecting HEK-293T, HepG2, Huh7, and THP-1 cells with SFTSV (MOI = 1) for 1 h, the cells were treated with QQGX at concentrations of

5 mg/mL (25 μL), and 10 mg/mL (50 μL), respectively. After 24 h, the cells were collected and lysed in RIPA solution. A total of 10 mL of protein solution was loaded onto 10% Tris-glycine SDS-polyacrylamide gels for electrophoresis. The proteins were then transferred onto a nitrocellulose membrane using an electrophoresis system and blocked with TBST (0.1% Tween-20 containing 5% skim milk). The membrane was probed with the NP antibody and the Tubulin antibody.

RNA extraction and qRT-PCR

Total cellular RNA was extracted by TRIzol (Qiagen, Germany, 79306) extraction. Using TransScript® II First-Strand cDNA Synthesis SuperMix (Yeasen Biotech, China, 11149ES10) to reverse transcribe RNA into cDNA using Random Primers N6. qRT-PCR assay was performed using 2 × HQ SYBR qPCR Mix (ZOMANBIO, China, ZF501), and mRNA levels were normalized to GAPDH. Results were analyzed as fold changes using the $2^{-\Delta\Delta Ct}$ method. The primer sequences used in the study are presented in Supplemental Table S5.

Determination of SFTSV titers

$TCID_{50}$ assay

Vero cells were plated in a 96-well plate and allowed to grow until they reached 80%–90% confluency. Subsequently, they were incubated for 4 h with 100 μL of SFTSV (MOI = 1) that had been serially diluted 10-fold, either alone or in combination with 10 mg/mL (50 μL) QQGX supernatant. After 4 h of viral adsorption, the supernatant was removed and replaced with fresh medium, followed by an additional 5-day incubation. For the negative control, an equivalent volume of DMEM was added instead of the viral solution, with eight replicates prepared for each dilution gradient. After incubation, cells from each well were collected for RNA extraction. The number of virus-positive wells at each dilution was determined by qRT-PCR detection of viral nucleic acids. Finally, the SFTSV titer was calculated using the Reed-Muench method.

Immunostaining plaque assay

Vero cells were seeded into a 24-well plate and allowed to grow until they reached 80%–90% confluency. The cells were then incubated with 400 μL of 10-fold serial dilutions of SFTSV, either alone or in combination with 10 mg/mL (50 μL) QQGX for 4 h. After incubation, the supernatant was removed, Then, 1 mL of DMEM supplemented with 1.1% sodium carboxymethyl cellulose (CMC) (Biotopped, China, 9004-32-4) and 2% FBS was added to each well. The cells were cultured for an additional 5 days, after which they were fixed with 4% paraformaldehyde (Solarbio, China, P1110). Following fixation, the cells were blocked for 2 h with 5% skim milk containing 0.2% Triton X-100 (diluted in TBST) (Solarbio, T8200). The cells were then incubated overnight at 4 °C with anti-NP serum (diluted 1:1000) (Primary antibodies specific for SFTSV NP were obtained from our laboratory). After three washes with PBS containing 0.05% Tween 20, the cells were incubated at room temperature for 1 h with HRP-conjugated anti-rabbit antibody (diluted 1:1000) (Proteintech, China, SA00001-2). Finally, viral plaques were stained using the enhanced HRP-DAB chromogenic substrate kit (TIANGEN, China, PA110), and virus titers were determined by counting plaque-forming units (PFUs).

Detection of QQGX effects on key cytokines

HEK-293T cells were cultured in a 24-well plate and infected with SFTSV (MOI = 1) when the cell density reached 80%. After 1 h of infection, the supernatant was removed, and 50 μL of 10 mg/mL QQGX was added to the cells, and the cells were then incubated for 48 h. Following incubation, the cell culture supernatant was collected and centrifuged at 1,000 ×*g* for 10 min for subsequent analysis. THP-1 cells were cultured in 24-well plates, pretreated with 50 μL of 10 mg/mL QQGX for 6 h, and then infected with SFTSV (MOI = 1). QQGX was maintained throughout the entire process. After 48 h, the cell culture supernatant and the cells were collected respectively. The cell culture supernatant was centrifuged at 1,000 ×*g* for 10 min. Subsequently, cytokine levels of IL-6, IL-10, TNF-α, and IL-1β were measured using ELISA kits (ABclonal, China, RK00004, RK00012, RK00030, RK05046) as the manufacturer's instructions. And the cells were used to extract RNA, mRNA expression levels of IL-6, IL-10, TNF-α, and IL-1β in cells were measured.

Cell synchronization

HEK-293T cells were synchronized in the G0/G1 phase by serum starvation for 24 h. To achieve S-phase synchronization, thymidine was added to the growth medium at a final concentration of 0.85 mM and incubated for 24 h. For G2/M phase synchronization, nocodazole was added to the growth medium at a concentration of 50 ng/mL and incubated for 24 h. Following synchronization, the cells were infected with SFTSV (MOI = 1) for 1 h and cultured in complete medium for 24 h. The cells were collected and analyzed by qRT-PCR.

Cell cycle analysis by flow cytometry

HEK-293T cells were infected with SFTSV (MOI = 1) for 1 h, then treated with QQGX at doses of 0, 2.5, 5, 7.5, or 10 mg/mL for 24 h. The cell cycle distribution (G0/G1, S, G2/M phases) was analyzed using flow cytometry. In a separate experiment, cells infected or uninfected with SFTSV (MOI = 1) were treated with 50 μL of 10 mg/mL QQGX or left untreated for 24 h, and then subjected to cell cycle analysis. After the cells were thoroughly digested with RNase A and stained with propidium iodide (PI), their cell cycle distribution was analyzed using a cell cycle analysis kit, following the manufacturer's instructions (Solarbio, CA1510). The PI-stained cells were examined using a BD FACSCalibur automated multicolor flow cytometer (FACScan; BD), and at least 15,000 cells were counted per sample. Data analysis was performed using ModFit LT software, version 2.0 (Verity Software House).

Bio-layer interferometry assay

All assays were run on an Octet Red 96 instrument according to a previously established method. The CDK2 and CCNA2 proteins were biotinylated and diluted to a concentration of 50 μg/mL prior to immobilization onto SSA sensors. The sensors were subsequently blocked, washed, and transferred to wells containing varying concentrations of the test compound, luteolin, in kinetic buffer. Default program settings for protein and small molecule binding were applied. Binding signals were recorded and analyzed using OctetHT V10.0 software. The R^2 value, which estimates the goodness of fit, approached 1, indicating an excellent fit.

Mouse liver bile ductal organoids culture

Biliary ducts were isolated from 6 to 8-week-old mice. Following the manufacturer's detailed instructions (Absin, China, abs9516), the pieces were incubated with pre-warmed digestion medium for 30 min on shaker at 37 °C. After digestion, the pieces were filtered through a 100 μm sieve, and the filtrate was collected. The supernatant was centrifuged at 300 ×*g* for 5 min and discarded. Then, buffer B was added and the pellet was resuspended for further centrifugation. Subsequently, the bile ducts were collected, embedded in Matrix-Gel, and seeded on a 24-well plate. The process of expanding mouse liver bile ductal organoids in culture involved gently blowing the matrix adhesive and collecting it in a 15 mL centrifuge tube. After digestion and centrifugation, the organoids were collected and securely embedded within Matrix-Gel. Primary organoids were passaged after 7 days of culture, and the passaged organoids reached a diameter of 200–300 μm within 4 days. After QQGX pretreatment, organoids reaching 200–300 μm in size were infected with 50

μL of SFTSV (7.2×10^7 $TCID_{50}$/mL), achieving a final concentration of 7.2×10^6 $TCID_{50}$/mL. Subsequent changes in organoid size were monitored.

Statistical analysis

All results were analyzed with GraphPad Prism and were presented as means ± standard deviations (SD). The two-tailed Student's unpaired *t*-test and multiple *t*-test were used to determine statistical significance.

DATA AVAILABILITY

All the data generated in the current study are included in the manuscript. The raw data supporting the conclusions of this article will be made available by the authors, without undue reservation.

ETHICS STATEMENT

Balb/c mice (6–8 weeks, SPF level), purchased from China Huafukang. All the animal experiments involved in this work were approved by the Animal Ethics Committee of Tianjin University (Approval No.: TJUE-2024-362).

AUTHOR CONTRIBUTIONS

Xixi Shi: conceptualization, data curation, formal analysis, visualization, writing - original draft, writing -review&editing. Zining Wang: conceptualization, formal analysis, investigation, visualization, writing - original draft, writing - review&editing. Zixiang Liu: formal analysis, funding acquisition, investigation, visualization, writing - original draft, writing - review&editing. Qinting Lin: methodology, project administration. Mengqian Huang: methodology. Tze Yean Lim: resources. Xiaoyan Li: project administration. Tao Wang: data curation, funding acquisition, investigation, resources, supervision, visualization, writing - original draft, writing - review&editing.

CONFLICT OF INTEREST

All authors declare that they have no competing interests exist.

ACKNOWLEDGEMENTS

This work was supported by the National Natural Science Foundation of China (32170144 and 32470146).

APPENDIX A. SUPPLEMENTARY DATA

Supplementary data to this article can be found online at https://doi.org/10.1016/j.virs.2025.03.011.

REFERENCES

Baba, M., Okamoto, M., Toyama, M., Sakakibara, N., Shimojima, M., Saijo, M., Niwa, T., Yagi, Y., 2023. Amodiaquine derivatives as inhibitors of severe fever with thrombocytopenia syndrome virus (SFTSV) replication. Antivir. Res. 210, 105479.

Boezio, B., Audouze, K., Ducrot, P., Taboureau, O., 2017. Network-based approaches in pharmacology. Mol. Inform. 36, 1700048.

Chen, C.C., Qin, X.M., Du, G.H., Zhou, Y.Z., 2019. The "compatible art" of effective components from traditional Chinese medicine: research on the compatibility and proportion of effective components. Acta Pharm. Sin. 54, 808–817.

Clevers, H., 2016. Modeling development and disease with organoids. Cell 165, 1586–1597.

Corrò, C., Novellasdemunt, L., Li, V.S.W., 2020. A brief history of organoids. Am. J. Physiol. Cell Physiol. 319, C151–c165.

Davy, C., Doorbar, J., 2007. G2/M cell cycle arrest in the life cycle of viruses. Virology 368, 219–226.

Ding, J., Li, J., Zhang, Z., Du, Y., Liu, Y., Wang, P., Du, H., 2023. Network pharmacology combined with metabolomics to explore the mechanism for Lonicerae Japonicae flos against respiratory syncytial virus. BMC Complement Med Ther 23, 449.

Dutta, D., Heo, I., Clevers, H., 2017. Disease modeling in stem cell-derived 3D organoid systems. Trends Mol. Med. 23, 393–410.

Efferth, T., Li, P.C., Konkimalla, V.S., Kaina, B., 2007. From traditional Chinese medicine to rational cancer therapy. Trends Mol. Med. 13, 353–361.

Feuer, R., Mena, I., Pagarigan, R., Slifka, M.K., Whitton, J.L., 2002. Cell cycle status affects coxsackievirus replication, persistence, and reactivation in vitro. J. Virol. 76, 4430–4440.

Frazzi, R., 2021. BIRC3 and BIRC5: multi-faceted inhibitors in cancer. Cell Biosci. 11, 8.

Gearhart, T.L., Bouchard, M.J., 2010. Replication of the hepatitis B virus requires a calcium-dependent HBx-induced G1 phase arrest of hepatocytes. Virology 407, 14–25.

Gu, X.L., Su, W.Q., Zhou, C.M., Fang, L.Z., Zhu, K., Ma, D.Q., Jiang, F.C., Li, Z.M., Li, D., Duan, S.H., Peng, Q.M., Wang, R., Jiang, Y., Han, H.J., Yu, X.J., 2022. SFTSV infection in rodents and their ectoparasitic chiggers. PLoS Neglected Trop. Dis. 16, e0010698.

Guo, X., Zhang, L., Zhang, W., Chi, Y., Zeng, X., Li, X., Qi, X., Jin, Q., Zhang, X., Huang, M., Wang, H., Chen, Y., Bao, C., Hu, J., Liang, S., Bao, L., Wu, T., Zhou, M., Jiao, Y., 2013. Human antibody neutralizes severe Fever with thrombocytopenia syndrome virus, an emerging hemorrhagic Fever virus. Clin. Vaccine Immunol. 20, 1426–1432.

Ji, M., Hu, J., Zhang, D., Huang, B., Xu, S., Jiang, N., Chen, Y., Wang, Y., Wu, X., Wu, Z., 2024. Inhibition of SFTSV replication in humanized mice by a subcutaneously administered anti-PD1 nanobody. EMBO Mol. Med. 16, 575–595.

Jung, S.I., Kim, Y.E., Yun, N.R., Kim, C.M., Kim, D.M., Han, M.A., Kim, U.J., Kim, S.E., Kim, J., Ryu, S.Y., et al., 2021. Effects of steroid therapy in patients with severe fever with Thrombocytopenia syndrome: a multicenter clinical cohort study. PLoS Neglected Trop. Dis. 15, e0009128.

Kang, S.Y., Yoo, J.R., Park, Y., Kim, S.H., Heo, S.T., Park, S.H., Kim, M., Kim, T.J., Oh, S., Lee, M.S., Kim, J.M., Cho, N.H., Lee, K.M., Lee, K.H., 2023. Fatal outcome of severe fever with thrombocytopenia syndrome (SFTS) and severe and critical COVID-19 is associated with the hyperproduction of IL-10 and IL-6 and the low production of TGF-β. J. Med. Virol. 95, e28894.

Kim, K.H., Kim, J., Ko, M., Chun, J.Y., Kim, H., Kim, S., Min, J.Y., Park, W.B., Oh, M.D., Chung, J., 2019. An anti-Gn glycoprotein antibody from a convalescent patient potently inhibits the infection of severe fever with thrombocytopenia syndrome virus. PLoS Pathog. 15, e1007375.

Kuchta, K., Cameron, S., Lee, M., Cai, S.Q., Shoyama, Y., 2022. Which East Asian herbal medicines can decrease viral infections? Phytochem. Rev. 21, 219–237.

Li, D., Saldanha, F.J.D., 2008. Clinical analysis of acupuncture combined with Chinese patent medicine in the treatment of dengue fever. Practical Tradit Chinese Med 24 (9), 553–554.

Li, H., Zhang, L.K., Li, S.F., Zhang, S.F., Wan, W.W., Zhang, Y.L., Xin, Q.L., Dai, K., Hu, Y.Y., Wang, Z.B., et al., 2019. Calcium channel blockers reduce severe fever with thrombocytopenia syndrome virus (SFTSV) related fatality. Cell Res. 29, 739–753.

Li, Q., Jia, C., Wu, H., Liao, Y., Yang, K., Li, S., Zhang, J., Wang, J., Li, G., Guan, F., Leung, E., Yuan, Z., Hua, Q., Pan, R.Y., 2022. Nao Tan Qing ameliorates Alzheimer's disease-like pathology by regulating glycolipid metabolism and neuroinflammation: a network pharmacology analysis and biological validation. Pharmacol. Res. 185, 106489.

Lim, S., Kaldis, P., 2013. Cdks, cyclins and CKIs: roles beyond cell cycle regulation. Development 140, 3079–3093.

Liu, S., Liu, H., Kang, J., Xu, L., Zhang, K., Li, X., Hou, W., Wang, Z., Wang, T., 2020. The severe fever with thrombocytopenia syndrome virus NSs protein interacts with CDK1 to induce G(2) cell cycle arrest and positively regulate viral replication. J. Virol. 94, e01575-19.

Lu, Q.B., Zhang, S.Y., Cui, N., Hu, J.G., Fan, Y.D., Guo, C.T., Qin, S.L., Yang, Z.D., Wang, L.Y., Wang, H.Y., Zhang, X.A., Liu, W., Cao, W.C., 2015. Common adverse events associated with ribavirin therapy for Severe Fever with Thrombocytopenia Syndrome. Antivir. Res. 119, 19–22.

Luo, N., Li, M., Xu, M., Shi, C., Shi, X., Ni, R., Chen, Y., Zheng, L., Tu, Y., Hu, D., Yu, C., Li, Q., Lu, Y., 2023. Research progress of fever with thrombocytopenia syndrome. Intensive Care Res 1–10. https://doi.org/10.1007/s44231-023-00035-6.

Muhammad, J., Khan, A., Ali, A., Fang, L., Yanjing, W., Xu, Q., Wei, D.Q., 2018. Network pharmacology: exploring the resources and methodologies. Curr. Top. Med. Chem. 18, 949–964.

Sakaguchi, K., Koga, Y., Yagi, T., Nakahara, T., Todani, M., Fujita, M., Tsuruta, R., 2019. Severe fever with thrombocytopenia syndrome complicated with pseudomembranous Aspergillus tracheobronchitis in a patient without apparent risk factors for invasive aspergillosis. Intern. Med. 58, 3589–3592.

Sehgal, A., Mehta, S., Sahay, K., Martynova, E., Rizvanov, A., Baranwal, M., Chandy, S., Khaiboullina, S., Kabwe, E., Davidyuk, Y., 2023. Hemorrhagic fever with renal syndrome in asia: history, pathogenesis, diagnosis, treatment, and prevention. Viruses 15, 561.

Seo, J.W., Kim, D., Yun, N., Kim, D.M., 2021. Clinical update of severe fever with thrombocytopenia syndrome. Viruses 13, 1213.

Singh, S., Numan, A., Sharma, D., Shukla, R., Alexander, A., Jain, G.K., Ahmad, F.J., Kesharwani, P., 2022. Epidemiology, virology and clinical aspects of hantavirus infections: an overview. Int. J. Environ. Health Res. 32, 1815–1826.

Su, W.Y., Lo, H.H., Wen, Y.L., Lu, J.W., Yen, I.C., Ho, Y.J., Kao, L.T., 2025. Assessing traditional Chinese medicines for anti-dengue using a national Health insurance research database and bioassays. Food Sci. Nutr. 13, e70009.

Sun, Y., Jin, C., Zhan, F., Wang, X., Liang, M., Zhang, Q., Ding, S., Guan, X., Huo, X., Li, C., Qu, J., Wang, Q., Zhang, S., Zhang, Y., Wang, S., Xu, A., Bi, Z., Li, D., 2012. Host cytokine storm is associated with disease severity of severe fever with thrombocytopenia syndrome. J. Infect. Dis. 206, 1085–1094.

Suo, T., Wang, H., Li, Z., 2016. Application of proteomics in research on traditional Chinese medicine. Expert Rev. Proteomics 13, 873–881.

Tani, H., Fukuma, A., Fukushi, S., Taniguchi, S., Yoshikawa, T., Iwata-Yoshikawa, N., Sato, Y., Suzuki, T., Nagata, N., Hasegawa, H., Kawai, Y., Uda, A., Morikawa, S., Shimojima, M., Watanabe, H., Saijo, M., 2016. Efficacy of T-705 (favipiravir) in the treatment of infections with lethal severe fever with thrombocytopenia syndrome virus. mSphere 1, e00061. -15.

Tani, H., Komeno, T., Fukuma, A., Fukushi, S., Taniguchi, S., Shimojima, M., Uda, A., Morikawa, S., Nakajima, N., Furuta, Y., Saijo, M., 2018. Therapeutic effects of favipiravir against severe fever with thrombocytopenia syndrome virus infection in a lethal mouse model: dose-efficacy studies upon oral administration. PLoS One 13, e0206416.

Verbeeck, R.K., 2008. Pharmacokinetics and dosage adjustment in patients with hepatic dysfunction. Eur. J. Clin. Pharmacol. 64, 1147–1161.

Wang, X., Wang, Z.Y., Zheng, J.H., Li, S., 2021. TCM network pharmacology: a new trend towards combining computational, experimental and clinical approaches. Chin. J. Nat. Med. 19, 1–11.

Wu, Y., Xiong, J., Zhao, X., Mei, Y., Jiang, H., 2024. Conducted a Clinical Study on the Treatment of Acute Stage Bronchial Asthma in Children with Damp Heat Syndrome Using Ganlu Disinfectant Pill Combined with Acupoint Application, 45, pp. 51–53, 05.

Yan, C., Niu, Y., Wang, X., 2022. Blood transcriptome analysis revealed the crosstalk between COVID-19 and HIV. Front. Immunol. 13, 1008653.

Yang, M., Sheng, Q., Ge, S., Song, X., Dong, J., Guo, C., Liao, L., 2023. Mutations and clinical characteristics of dRTA caused by SLC4A1 mutations: analysis based on published patients. Front Pediatr 11, 1077120.

Yoo, J.R., Kim, T.J., Heo, S.T., Hwang, K.A., Oh, H., Ha, T., Ko, H.K., Baek, S., Kim, J.E., Kim, J.H., Lee, J., Kang, M.J., Yoo, M.S., Kim, J.M., Lee, K.M., Lee, K.H., 2021. IL-6 and IL-10 levels, rather than viral load and neutralizing antibody titers, determine the fate of patients with severe fever with thrombocytopenia syndrome virus infection in South Korea. Front. Immunol. 12, 711847.

Zhang, C., Quan, Y., Yang, L., Bai, Y., Yang, Y., 2022. 6-Methoxyflavone induces S-phase arrest through the CCNA2/CDK2/p21CIP1 signaling pathway in HeLa cells. Bioengineered 13, 7277–7292.

Zhao, L., Zhang, H., Li, N., Chen, J., Xu, H., Wang, Y., Liang, Q., 2023. Network pharmacology, a promising approach to reveal the pharmacology mechanism of Chinese medicine formula. J. Ethnopharmacol. 309, 116306.